

Can the 21 cm signal probe Population III and II star formation?

Hidenobu Yajima^{1,2*} and Sadegh Khochfar¹

¹ SUPA†, Institute for Astronomy, University of Edinburgh, Royal Observatory, Edinburgh, EH9 3HJ, UK

² Department of Earth & Space Science, Graduate School of Science, Osaka University, 1-1 Machikaneyama, Toyonaka, Osaka 560-0043, Japan

Accepted ?; Received ??; in original form ???

ABSTRACT

Using varying models for the star formation rate (SFR) of Population (Pop) III and II stars at $z > 6$ we derive the expected redshift history of the global 21 cm signal from the inter-galactic medium (IGM). To recover the observed Thomson scattering optical depth of the cosmic microwave background (CMB) requires SFRs at the level of $\sim 10^{-3} M_{\odot} \text{ yr}^{-1} \text{ Mpc}^{-3}$ at $z \sim 15$ from Pop III stars, or $\sim 10^{-1} M_{\odot} \text{ yr}^{-1} \text{ Mpc}^{-3}$ at $z \sim 7$ from Pop II stars. In the case the SFR is dominated by Pop III stars, the IGM quickly heats above the CMB at $z \gtrsim 12$ due to heating from supernovae. In addition, Ly α photons from haloes hosting Pop III stars couple the spin temperature to that of the gas, resulting in a deep absorption signal. If the SFR is dominated by Pop II stars, the IGM slowly heats and exceeds the CMB temperature at $z \sim 10$. However, the larger and varying fraction of Pop III stars is able to break this degeneracy. We find that the impact of the initial mass function (IMF) of Pop III stars on the 21 cm signal results in an earlier change to a positive signal if the IMF slope is ~ -1.2 . Measuring the 21 cm signal at $z \gtrsim 10$ with next generation radio telescopes such as the Square Kilometre Array will be able to investigate the contribution from Pop III and Pop II stars to the global star formation rate.

Key words: diffuse radiation – dark ages, reionization, first stars – stars: Population II – galaxies: high-redshift – galaxies: formation

1 INTRODUCTION

The star formation history (SFH) of galaxies and the physical state of the intergalactic medium (IGM) at $z \geq 6$ is of key importance to understand the transition of the Universe from a neutral to highly ionized state and the sources responsible for it. The observational situation has made significant progress over the recent years. The Thomson scattering optical depth of the cosmic microwave background (CMB) suggest that the IGM was re-ionized by $z \sim 11$ (Komatsu et al. 2011; Planck Collaboration XVI 2014). In addition, Ly α emitters allow to estimate the degree to which the IGM is re-ionized at $z \sim 7$ (Ota et al. 2008; Kashikawa et al. 2006, 2011). As for the galaxy population, the *Hubble Space Telescope* (HST) with Wide Field Camera 3 (WFC3) allowed to derive stellar masses and star formation rates for galaxies at $z > 6$ (e.g., McLure et al. 2011; Bouwens et al. 2012). These are complemented by afterglow measurements of γ -ray burst, which suggest similar

cosmic star formation histories at $z \sim 6 - 8$ (Yüksel et al. 2008; Kistler et al. 2009, 2013). Despite these successes, the physical interpretation of the observations is still partly degenerate as to the detailed redshift evolution of the SFH and physical state of the IGM at $z \geq 6$. This is mainly because the CMB observations are interpreted assuming instantaneous reionization, and observations of the galaxy population only probe the bright-end ($> L_{*}$) of the luminosity function at high redshifts securely (Ono et al. 2012; Shibuya et al. 2012; Finkelstein et al. 2013). Moreover, the SFH of Population (Pop) III stars and their impact on the IGM is very complex. Despite recent state-of-the-art simulations of Pop III stars formation (e.g. Yoshida et al. 2008; Turk et al. 2009; Clark et al. 2011; Stacy et al. 2012; Wise et al. 2012a; Ahn et al. 2012; Umemura et al. 2012; Susa 2013; Hirano et al. 2014; Stacy & Bromm 2014), understanding of their formation over a wide range of physical conditions and redshift range ($z = 6 - 30$) is still lacking. One promising way to resolve these issues is the observation of the 21 cm line from the IGM at $z > 6$ by the LOW Frequency Array (LOFAR; Harker et al. 2010), the Murchison Widefield Array (MWA; Lonsdale et al. 2009), and the

* E-mail: yajima@roe.ac.uk (HY)

† Scottish Universities Physics Alliance

Square Kilometre Array (SKA; Dewdney et al. 2009). For example, LOFAR covers $z \lesssim 11$ with the angular resolution of $\sim 3''$, and SKA will cover more wide range surveys at $z \lesssim 19$ with a higher resolution of $\sim 1''$.

The 21 cm emission is sensitive to the ionization state of hydrogen, gas temperature and the Ly α radiation field, which are controlled by the first stars, galaxies, and quasars (QSOs) (Yajima & Li 2014). Previous works has addressed the detailed structures of 21 cm emission around Pop III stars (Chen & Miralda-Escudé 2004, 2008; Tokutani et al. 2009; Yajima & Li 2014), galaxies (McQuinn et al. 2006; Mellema et al. 2006; Kuhlen et al. 2006; Wyithe & Loeb 2007; Semelin et al. 2007; Baek et al. 2009; Mesinger et al. 2011; Iliev et al. 2012), and QSOs (Wyithe et al. 2005; Geil & Wyithe 2008; Alvarez et al. 2010; Datta et al. 2012; Yajima & Li 2014). Their work suggests that future observations are able to resolve the 21 cm structure around giant HII region made by massive galaxies like QSO hosts, while it will be difficult to detect individual sources around typical galaxies or Pop III stars (Yajima & Li 2014). The distribution of giant HII bubbles as probed by 21 cm observation will thus give us valuable information about structure formation and cosmology (see also, Chongchitnan & Silk 2012).

An alternative approach is to focus on the redshift history of the global 21 cm emission, focusing on the spatially averaged value instead (Furlanetto 2006; Pritchard & Loeb 2008; Mirocha et al. 2013). Instead of the detailed structure around sources, the global signal reflects the statistical nature of stars and the IGM, e.g., the global star formation history of Pop II & III stars, the mean degree of ionization and temperature of the IGM, and the mean intensity of Ly α radiation. Previous studies investigated the redshift evolution of the differential brightness temperature (δT_b) with different free parameters for the heating rate and SFR (Pritchard & Loeb 2008). In this work, we revisit earlier attempts by taking into account recent progresses on cosmic reionization and the star formation history of galaxies. We construct models that match the latest observations, and investigate effects of Pop II & III stars on the redshift history of the global 21 cm emission.

Our paper is organized as follows. We describe our model in Section 2. In Section 3, we show the redshift evolution of the ionization degree, temperature, and 21 cm signal of the IGM. In Section 4, we investigate the effects of black holes and initial mass function of Pop III stars on the 21 cm signal. Finally, in Section 5, we summarise our main conclusions.

2 MODEL

In the following sections we lay out our model assumptions. Throughout this paper we use the cosmological parameters $\Omega_M = 0.26$, $\Omega_\Lambda = 0.74$ and $h = 0.72$ as inferred by the WMAP 7-year data (Komatsu et al. 2011), which are consistent with the results of the Planck mission (Planck Collaboration XVI 2014), and do not change the results of our study significantly.

2.1 Star formation history

We start by constructing models of the Pop II and III SFH. A common fit to the Pop II SFRD is given in Bouwens et al. (2011) as:

$$\dot{M}_*^{\text{PopII}} = (a + bz)h / [1 + (z/c)^d] M_\odot \text{ yr}^{-1} \text{ Mpc}^{-3} \quad (1)$$

where (a, b, c, d) are fitting parameters, with best fitting values $a = 0.017$, $b = 0.13$, $c = 3.3$ and $d = 5.3$. In the following we will refer to this as our fiducial model. There is some degree of discussion as to the appropriate values for the free parameters. For example, $d = 7$ fits the SFRD from the galaxy population reported in Oesch et al. (2013), while $c = 4.5$ matches GRBs observations by Yüksel et al. (2008); Kistler et al. (2009, 2013). The latter discrepancy has been argued is a result of GRBs probing star formation rates in galaxies below the detection limit of surveys. Integrating the observed luminosity function of galaxies under the assumption of a faint-end slope $\alpha \sim -1.7$ down to $L = 0$ brings both estimates in agreement. We, however note that the faint-end slope is highly uncertain within the current detection limits of galaxy observations (e.g., Khochfar et al. 2007; McLure et al. 2011) and the simple fit to the luminosity function may be broken at low luminosity due to the strong suppression of star formation in low-mass galaxies by radiative and supernovae feedback (Wise et al. 2012b; Hasegawa & Semelin 2013). In addition, the sample of GRBs at $z > 6$ is still very small (\sim a few). Therefore, considering the uncertainties, we investigate two alternative star formation models, a high star formation model (Pop Iib) with $d = 7.0$ and a low one (Pop Iic&d) with $c = 4.5$. Moreover, recent galaxy observations suggested that SFRD steeply decreases with increasing redshift at $z > 8$ (e.g., Oesch et al. 2013). Theoretical modeling based on the collapse fraction of haloes showed SFRD falls exponentially at high-redshift (e.g., Pritchard & Loeb 2010; Mirocha et al. 2013). Therefore, as an additional model, we consider the exponential decay model (PopIie) at $z > 8$ with $\text{SFRD} = b \times \exp(-a \times z)$ where a and b are fitting parameters. The PopIie model follows PopIIa at $z \leq 8$. The fitting parameters are chosen to match the observational data by Oesch et al. (2013, 2014), and they are $a = 1.6$ and $b = 7.0$ respectively. A summary of the models is listed in Table 1. The number of Ly α and ionizing photons emitted from the source stars is computed based on the theoretical spectral energy distribution (SED) given by the population synthesis code PÉGASE v2.0 (Fioc & Rocca 1997) with a metallicity of $Z = 10^{-2} Z_\odot$ (e.g., Wise et al. 2012b) and Salpeter IMF.

On the other hand, for the Pop III stars, the Ly α and ionizing photon emissivities are not sensitive to the IMF, it is roughly proportional to total stellar mass alone, because the effective temperature is almost constant at $T \sim 10^5$ K and the luminosity scales close to linearly with the mass (Bromm et al. 2001b). Hence we use the ionizing photon emissivity of $120 M_\odot$ stars derived by Schaerer (2002) and estimate the total ionizing photon emissivity per solar mass by dividing by $120 M_\odot$, and assume the effective temperature of $T = 10^5$ K to estimate Ly α photons from stellar continuum radiation. In addition, there are no strong observational constraints on the PopIII SFR. In the case of Pop III stars, their formation rate is reduced due to metal enrichment by supernovae (e.g., Omukai et al. 2008; Maio et al.

2011; Wise et al. 2012b; Johnson et al. 2013). As a result, the SFRD of Pop III stars might have a peak at a specific redshift. Hence, we use the simple exponential decay model with a peak at the typical Pop III star forming redshift $z = 15$ (e.g., Yoshida et al. 2008; Johnson et al. 2013) as follows,

$$\dot{M}_*^{\text{PopIII}} = A \times \exp(-|z - 15|/B) M_\odot \text{ yr}^{-1} \text{ Mpc}^{-3} \quad (2)$$

where A and B are again fitting parameters. The parameter “ A ” is the amplitude factor, and the “ B ” controls the steepness of the redshift dependence. Even with state-of-the-art simulations of Pop III stars, there is a large room in the mean values and redshift evolution, because of the difficulties to resolve the initial mass function, the metal/dust enrichment and radiative/supernovae feedback. Recent radiative hydrodynamics simulations show a weak redshift evolution with SFRD $\sim 10^{-4} - 10^{-5} M_\odot \text{ yr}^{-1}$ (Wise et al. 2012b). Therefore, we consider slow redshift evolution models ($B = 10.0$) with a high SFRD (PopIIIa: $A = 10^{-3}$) and a lower one (PopIIIc: $A = 10^{-5}$). In addition, we construct a rapid redshift evolution model (PopIIIb) with $A = 10^{-2}$ and $B = 1.0$. These star formation models are shown in Figure 1. We see the SFHs of Pop II stars satisfy recent observations. In addition, recent cosmological simulations by Johnson et al. (2013) including supernova feedback predict star formation rates similar to those assumed by our models. The bottom panel of the Figure 1 shows the cumulative stellar mass as a function of redshift. Current observation are still highly uncertain at $z \gtrsim 6$. Note that we here estimate the stellar mass by integrating the SFRD. Our PopIIa or PopIIb models roughly recover the observed stellar mass density (SMD) at $z \leq 8$, while they are above the observed ones at $z \sim 10$. However, the SMD at $z \sim 10$ was estimated from only four bright galaxies. Therefore, there is a large uncertainty in the contribution from low-mass galaxies. If the faint-end slope is steeper, the SMD can increase significantly. The PopIIe follows the observed SMD at $z \sim 5 - 10$. In the case of massive Pop III stars, their life times are short and they end as either Type-II supernovae or direct collapse to black holes (Heger & Woosley 2002). As a result, the Pop III cumulative mass is an overestimate of the actual stellar mass.

The SFRD in model PopIIa is higher than that of PopIIb and PopIIIc at $z \gtrsim 18$ in contrast to expectations from models. However, the contribution of PopII stars in this model towards cosmic reionization and the 21 cm signal at $z \gtrsim 18$ is negligible and does not impact our conclusions. For the PopIIa+PopIIIb model, we turn off the formation of Pop II stars when the SFRD of Pop II stars is higher than that of Pop III stars at $z \gtrsim 18$.

2.2 Ionization history

Based on the above models for the SFRD, we derive cosmic reionization histories. Some fraction of ionizing photons from stars can escape from halos and ionize the surrounding IGM (Hasegawa & Semelin 2013; Paardekooper et al. 2013). Recent theoretical work shows the escape fraction is ~ 0.2 for typical galaxies (Yajima et al. 2009, 2011, 2014; Razoumov & Sommer-Larsen 2010), and ~ 0.5 for dwarf galaxies or Pop III stars (Abel et al. 2007; Whalen et al. 2004; Kitayama et al. 2004; Paardekooper et al. 2013). Here, we assume $f_{\text{esc}} = 0.5$ for Pop III stars and $f_{\text{esc}} = 0.2$

for Pop II stars for our fiducial models, and $f_{\text{esc}} = 0.5$ for one additional model of the Pop II SFH (PopIIId). Using these models the redshift evolutions of volume fraction of HII region is calculated as (Barkana & Loeb 2001):

$$\frac{dQ_{\text{HII}}}{dt} = \frac{1}{n_{\text{H}}^0} \dot{n}_{\text{Ion}}^\gamma - \alpha_{\text{B}} C (1+z)^3 n_{\text{H}}^0 Q_{\text{HII}} \quad (3)$$

where Q_{HII} is the volume fraction of HII, n_{H}^0 is the present-day hydrogen number density ($\sim 1.9 \times 10^{-7} \text{ cm}^{-3}$), $\dot{n}_{\text{Ion}}^\gamma$ is a number density of the escaped ionizing photon, α_{B} is the case-B recombination rate, and C is a clumpiness factor of IGM. We assume the recombination rate at $T = 10^4 \text{ K}$ ($\alpha_{\text{B}} = 2.59 \times 10^{-13} \text{ cm}^3 \text{ s}^{-1}$) and $C = 3$ which is suggested by numerical simulations (Pawlik et al. 2009; Jeon et al. 2014). Free electrons produced by cosmic reionization contributes to the Thomson scattering optical depth (τ_{e}) in CMB observations which is estimated by

$$\tau_{\text{e}} = \int_0^\infty \sigma_{\text{T}} n_{\text{e}}(z) c \left| \frac{dt}{dz} \right| dz, \quad (4)$$

where

$$\frac{dt}{dz} = \frac{1}{(1+z)H_0\sqrt{\Omega_{\text{M}}(1+z)^3 + \Omega_{\Lambda}}}. \quad (5)$$

In this work, we assume the single ionization rate of helium is the same as the one for hydrogen at $z \geq 3$, and the double ionization takes place at $z < 3$ (e.g., Wyithe et al. 2010; Inoue et al. 2013). Recent simulations show that indeed the fraction of HeII is close to the HII fraction at the high redshift, although the ionization fraction of helium is slightly lower than the one for hydrogen (Ciardi et al. 2012).

2.3 Thermal evolution

Before $z \sim 150$, the temperature of the gas is given by its coupling to the CMB via Compton scattering (Peebles 1993). Thereafter, gas starts to decouple from the CMB and the temperature decreases by adiabatic expansion $(1+z)^2$, while that of the CMB does as $(1+z)$. However, as structure grows, additional heating sources can form. In particular, X-ray photons can travel for long distance and partially ionize the IGM, and become important sources for the global 21 cm emission (Furlanetto 2006; Mirocha et al. 2013). To account for this we include the X-ray emission from supernovae as estimated in Furlanetto (2006),

$$L_{\text{X}}^{\text{SN}} = 1.6 \times 10^{40} f_{\text{e}} \left(\frac{\epsilon_{\text{e}}}{0.05} \frac{\nu_{\text{SN}}}{0.01 M_\odot^{-1}} \frac{E_{\text{SN}}}{10^{51} \text{ erg}} \frac{\text{SFR}}{1 M_\odot \text{ yr}^{-1}} \right) \text{ erg s}^{-1}, \quad (6)$$

where f_{e} is the deposited energy fraction from accelerated electrons in supernova shocks into X-ray energy, ϵ_{e} is the conversion fraction from total supernova energy to the acceleration of electrons, ν_{SN} is the number of supernovae per unit mass of star formation, and E_{SN} is the total supernova energy. Following Furlanetto (2006), we use the values of $f_{\text{e}} = 0.5$, $\epsilon_{\text{e}} = 0.05$, $\nu_{\text{SN}} = 0.01 M_\odot^{-1}$, $E_{\text{SN}} = 10^{51} \text{ erg}$ for Pop II stars. Hence, the X-ray luminosity from Pop II stars is simply given by $L_{\text{PopII,X}}^{\text{SN}} = 0.8 \times 10^{40} (\text{SFR}/M_\odot \text{ yr}^{-1}) \text{ erg s}^{-1}$. The typical mass of Pop III stars is likely to be much higher than that of Pop II due to the higher Jeans mass and accretion rate at their formation (e.g., Bromm et al. 2001a; Nakamura & Umemura

2001; Abel et al. 2002; Yoshida et al. 2008; Hosokawa et al. 2011; Umemura et al. 2012). Very recently, Hirano et al. (2014) suggested that the mass of Pop III stars significantly changes depending on the formation sites and that the initial mass function might be flat with the mass ranging from ~ 10 to $\sim 500 M_{\odot}$. Hence, ν_{SN} should be higher than $0.01 M_{\odot}^{-1}$ for Pop III stars. We here assume a flat shape with mass range $10 - 500 M_{\odot}$ giving $\nu_{\text{SN}} \sim 0.17$ (Heger & Woosley 2002). In addition, Pop III stars of $120 - 260 M_{\odot}$ end their lives as pair-instability supernovae with energies $\sim 10^{53}$ erg s $^{-1}$. As a result, the X-ray luminosity is estimated by $L_{\text{popIII,X}}^{\text{SN}} = 1.0 \times 10^{43} (\text{SFR}/M_{\odot} \text{ yr}^{-1})$ erg s $^{-1}$. In this work, we use the flat IMF in our fiducial model, and then investigate the impact of different IMF slopes on the 21 cm signal. The energy fraction from X-rays that goes into heating the IGM ($f_{\text{X,heat}}$) is estimated by $f_{\text{X,heat}} = 0.9971 [1 - (1 - x_{\text{HII}})^{1.3163}]$ (Shull & van Steenberg 1985). Considering the X-ray heating, the temperature evolution of HI gas is derived from (Maselli et al. 2003; Yajima & Li 2014)

$$\frac{dT_{\text{HI}}}{dt} = \frac{2}{3k_{\text{B}}n_{\text{H}}} \left[k_{\text{B}}T_{\text{HI}} \frac{dn_{\text{H}}}{dt} + \Gamma_{\text{X,heat}} \right], \quad (7)$$

where T_{HI} is the temperature of neutral hydrogen gas and $\Gamma_{\text{X,heat}}$ is the X-ray heating rate. The first term on the right hand side of the equation represents the cooling due to cosmic expansion. The contribution from supernovae to cosmic reionization is not significant (Johnson & Khochfar 2011). Hence we do not include the ionization by X-ray photons.

2.4 Ly α background radiation

With the onset of star formation the Ly α background field starts appearing. Ly α radiation plays a key roll in determining the spin temperature via the Wouthuysen-Field effect (Wouthuysen 1952; Field 1958; Hirata 2006). There are mainly two sources of Ly α radiation, one is due to the recombination processes in HII regions, another is stellar continuum radiation in the frequency range from the Lyman-limit to Ly α . Stellar continuum radiation contributes to Ly α photons via the transition to the higher levels of the Lyman series (Ly γ , Ly δ ...) and cascade decay passing through from the 2p to the 1s state or the frequency shift to Ly α by cosmological redshifting. Previous studies of the global 21 cm emission, only took into account continuum stellar radiation from PopII because of its dominant contribution with respect to recombinations in the IGM or haloes. However, in the case of Pop III stars, the Ly α luminosity from the recombination process is larger than that of the continuum radiation due to the high effective temperature (Bromm et al. 2001b) of the star. In addition, due to the small size of HII regions (\sim kpc), Ly α photons can be efficiently scattered at the outer HI edge (Yajima & Li 2014). On the other hand, during the era when Pop II stars are dominant sources of ionization, the typical size of HII bubble can be larger (Iliev et al. 2012; Wise et al. 2012b). Therefore, Ly α photons from haloes may travel in the neutral IGM without scatterings due to the large velocity offset by the Hubble flow. In this work, hence, we apply Ly α photons from haloes for the calculation of T_{S} when the SFRD of Pop III stars is higher than that of Pop II stars or $X_{\text{HII}} < 0.5$. However, note that, even at lower redshift $z \sim 7$, recent observation suggested a

large fraction of Ly α flux is scattered because of surrounding residual HI gas (Kashikawa et al. 2011). Theoretically, Laursen et al. (2011) showed that 0.8 of Ly α photons from galaxies at $z = 6.5$ were scattered by the IGM, despite most of the IGM was ionized. The IGM transmission to Ly α photons is complicated because of the inhomogeneous HI and velocity distribution around galaxies, hence it is still controversial. Here, we use this simple model and will investigate detailed effects of Ly α photons from haloes on the IGM by numerical simulations in future work. For Ly α photons from the recombination in the IGM, the position of sources can be close to neutral IGM patches, hence some of them are scattered even when the IGM is highly ionized. Hence, we consider Ly α photons from the IGM for all cases. This may overestimate the number of Ly α scattering per atom, however, the effect of Ly α photons from the IGM is negligible because the emissivity is quite small due to the long recombination time scale of the IGM as shown in the later section. Thus, we estimate the Ly α emissivity and its relation with the 21 cm signal as follows:

$$\epsilon_{\text{Ly}\alpha} = \epsilon_{\text{IGM}}^{\text{rec}} + \epsilon_{\text{ISM}}^{\text{rec}} + \epsilon_{\text{star}}^{\text{cont}} \quad (8)$$

where

$$\epsilon_{\text{IGM}}^{\text{rec}} = 0.68h\nu_{\alpha}n_{\text{H}}^2(1 + f_{\text{He}})\alpha_{\text{B}}Q_{\text{HII}}, \quad (9)$$

$$\epsilon_{\text{ISM}}^{\text{rec}} = 0.68h\nu_{\alpha}\dot{n}_{\text{Ion}}(1 - f_{\text{esc}}), \quad (10)$$

$$\epsilon_{\text{star}}^{\text{cont}} = f_{\text{conv}} \times \int_{912\text{\AA}}^{1216\text{\AA}} \frac{L_{\nu}}{h\nu} d\nu. \quad (11)$$

The $\epsilon_{\text{IGM}}^{\text{rec}}$, $\epsilon_{\text{ISM}}^{\text{rec}}$ and $\epsilon_{\text{star}}^{\text{cont}}$ are the Ly α emissivities from HII regions in the IGM, ISM, and the stellar continuum radiation, respectively. The ν_{α} is the Ly α frequency. The factor 0.68 is the average probability of $T = 10^4$ K gas that a recombination process emits a Ly α photon via the 2p-1s state transition. The f_{conv} is the conversion probability from the continuum to Ly α line, it is 0.63 for Pop III stars and 0.72 for Pop II stars (Pritchard & Furlanetto 2006). These different values are due to the different slope of SEDs at the frequencies between Ly α and Lyman limit. As explained above, $\epsilon_{\text{ISM}}^{\text{rec}} = 0$ for $\text{SFRD}(\text{Pop II}) > \text{SFRD}(\text{Pop III})$ or $X_{\text{HII}} > 0.5$. Note that, here Ly α photons from recombination in the IGM or ISM can be localized, compared to stellar continuum radiation. However, these recombinations are the dominant sources for Pop III stars, and HII bubbles made by Pop III stars are typically much smaller than the angular resolution of future 21 cm observation. Hence these photons can work on the global 21 cm emission signal. The mean values may differ between our simple model and coarse grained ones from detailed 21 cm structures around sources. We will investigate the detailed structure of 21 cm signal by using cosmological simulations in future work. In addition, even if Ly α photons are scattered by the surrounding IGM, the propagation distance from Pop III stars can be small during the early phase of their stellar evolution (Yajima & Li 2014). If so, the contribution of Ly α photons from the ISM to the global 21 cm signal can be negligible. Given the uncertainties we therefore also investigate the 21 cm signal without Ly α photon contribution from the ISM.

	a	b	c	d	f_{esc}
PopIIa	0.017	0.13	3.3	5.3	0.2
PopIIb	0.017	0.13	3.3	7.0	0.2
PopIIc	0.017	0.13	4.5	5.3	0.2
PopIId	0.017	0.13	4.5	5.3	0.5
PopIIe	1.6	7.0×10^{-3}	—	—	0.2

Table 1. Model parameters for the Pop II SFRD. For PopIIa-c, the parameters $a - d$ relate to the SFRD as a function of redshift via $\text{SFRD} = (a + bz)h / [1 + (z/c)^d]$. The parameters of PopIIe are used for the exponential decay model at $z > 8$ using $\text{SFRD} = b \times \exp(-az)$. At $z \leq 8$, the SFRD of the PopIIe is the same as for model PopIIa. The parameter f_{esc} is the escape fraction of ionizing photons from haloes.

The mean intensity is then estimated by

$$J_{\alpha} = \frac{\epsilon_{\text{Ly}\alpha} \times c}{4\pi}. \quad (12)$$

2.5 Spin temperature

Finally we derive the 21 cm flux by considering the ionization, temperature and Ly α radiation field estimated in above equations. The differential brightness temperature to CMB is estimated by (Furlanetto 2006),

$$\delta T_{\text{b}} = 28.1 \text{ mK } x_{\text{HII}}(1 + \delta) \left(\frac{1+z}{10} \right)^{\frac{1}{2}} \frac{T_{\text{s}} - T_{\text{CMB}}}{T_{\text{s}}} \quad (13)$$

where δ is the overdensity, T_{s} and T_{CMB} are the spin temperature and CMB temperature respectively. Since we focus on the spatial mean of the 21 cm emission, we assume $\delta = 0$. The spin temperature is changed by

$$T_{\text{s}}^{-1} = \frac{T_{\text{CMB}}^{-1} + x_{\alpha}^{-1}T_{\text{c}}^{-1} + x_{\text{C}}^{-1}T_{\text{gas}}^{-1}}{1 + x_{\alpha} + x_{\text{C}}} \quad (14)$$

where T_{C} is the color temperature of the Ly α line, T_{gas} is the kinetic temperature of the gas, x_{α} and x_{C} are the coupling coefficients of Ly α photon scattering and gas collision, respectively. These coefficients are estimated as (Hirata 2006)

$$x_{\alpha} = 1.81 \times 10^{11} (1+z)^{-1} S_{\alpha} J_{\alpha}, \quad (15)$$

$$x_{\text{C}} = \frac{T_{\star}}{A_{10} T_{\text{CMB}}} (C_{\text{H}} + C_{\text{p}} + C_{\text{e}}), \quad (16)$$

where S_{α} is the scattering amplitude factor, $T_{\star} = 0.068 \text{ K}$, $A_{10} = 2.85 \times 10^{-15} \text{ s}^{-1}$ is the spontaneous emission factor of the 21 cm transition, P_{α} is the number of scatterings of Ly α photons per atom per second, C_{H} , C_{p} and C_{e} are the de-excitation rates due to collision with neutral atoms, protons, and electrons, respectively. We use the fitting formula given by Hirata (2006) for the S_{α} and that by Liszt (2001) and Kuhlen et al. (2006) for the de-excitation rates.

Since T_{C} quickly settles into T_{gas} owing to the recoil effect of Ly α photon scattering, $T_{\text{C}} = T_{\text{gas}}$ is assumed in our calculations. The spin temperature depends sensitively on the coupling due to Ly α scattering and collision. When the coupling is strong, T_{s} becomes $\sim T_{\text{gas}}$.

	A	B	f_{esc}
PopIIIa	5×10^{-4}	10.0	0.5
PopIIIb	4×10^{-3}	1.0	0.5
PopIIIc	5×10^{-5}	10.0	0.5

Table 2. Model parameters for the Pop III SFRD. The SFRD is modeled as $\text{SFRD} = A \times \exp(-|z - 15|/B)$.

	τ_{e}	z_{tr}
PopIIa + PopIIIa	0.087	11.5
PopIIa + PopIIIb	0.095	15.2
PopIIa + PopIIIc	0.052	7.7
PopIIa	0.048	7.5
PopIId	0.086	10.4
PopIIe+PopIIIa	0.084	11.0
PopIIe	0.045	7.2

Table 3. Thomson scattering optical depths of different models. z_{tr} is redshift at when the IGM temperature exceeds the CMB.

3 RESULTS

3.1 Ionization history

Ionization histories of the IGM are shown in Figure 2. At $z > 15$, most of the IGM is in a neutral state for all models. At $z < 15$, the ionization history of the individual models starts deviating from each other depending on their star formation histories. In the cases of Pop II stars alone, the ionization degree monotonically increases with time. For example, the case of PopIId reaches $X_{\text{HII}} = 0.5$ at $z = 9.8$, while it is at $z = 6.4$ in the case of PopIIa, because the ionizing photon emissivity of PopIId is higher than that of PopIIa by factor ~ 5 . The ionization degree in the PopIIe model is very small at $z < 8$, then it catches up with that of PopIIa at $z \leq 8$. Inclusion of Pop III stars in general changes the ionization degree to higher values as they provide an additional source of ionizing photons, and shifts the redshift of reionization to higher z .

The PopIIa+PopIIIa model shows the IGM is started to be ionized earlier ($X_{\text{HII}} \sim 0.1$ at $z = 16.4$), then the ionization degree slowly evolves and reaches to $X_{\text{HII}} = 0.5$ at $z = 8.3$. In addition, the PopIIe+PopIIIa model also shows a similar ionization history. This is because the ionizing photon emissivity of Pop III stars is dominant at $z > 8.3$, and that of the Pop II stars becomes almost the same as that in the PopIIa model. In the case of PopIIa+PopIIIb, the ionization history shows the more complex evolution. Due to the strong peak of the SFR of PopIII stars, at $z \sim 14$ most of gas is highly ionized once. As the PopIII SFR decreases, the ionization fraction X_{HII} drops back to a moderately neutral state $X_{\text{HII}} \sim 0.24$ at $z = 8.6$. At $z < 8$, the IGM is highly ionized again due to the PopII stars ($X_{\text{HII}} \sim 0.5$ at $z = 6.6$). In addition, despite the redshift evolution of the PopIII SFR is symmetric with a maximum at $z = 15$, the redshift evolu-

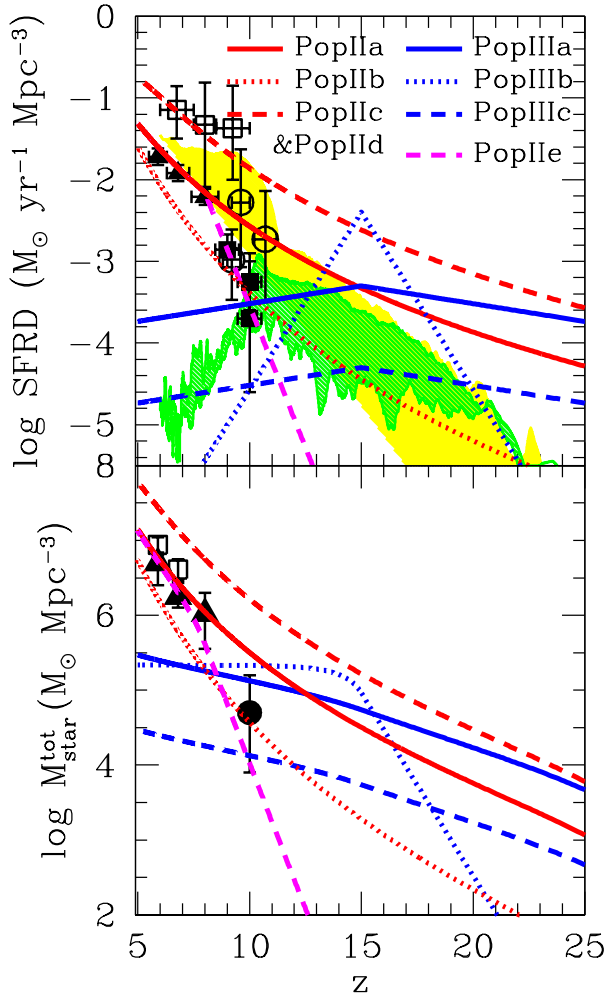


Figure 1. *Upper panel:* Redshift evolution of cosmic star formation rate density. Different lines represent different star formation models shown in Table 1 and Table 2. Symbols show the observational data. Filled triangles are from Bouwens et al. (2007, 2012), and filled squares are from Oesch et al. (2013, 2014). Open circles are from CRASH cluster detections (Bouwens et al. 2014; Zheng et al. 2012; Coe et al. 2013). Open squares are derived from gamma-ray bursts (Kistler et al. 2013). Green and yellow shade regions represents the star formation rate densities of Pop III and II stars respectively, calculated in the cosmological simulations by Johnson et al. (2013). The range of y-axis shows the models with or without the Lyman-Werner UV background which can suppress formation of hydrogen molecules. *Lower panel:* Cumulative stellar mass density of Pop III and II stars with different models. Symbols represent the observational data from González et al. (2011, open squares), Stark et al. (2013, filled triangles), and Oesch et al. (2014, filled circle).

tion of X_{HII} is asymmetric. This is because of contribution by Pop II stars and the lower recombination rate at lower redshift which is $\propto (1+z)^6$. In the case of PopIIa+PopIIIc, the contribution by PopIII stars is not significant. The ionization is somewhat enhanced by PopIII stars at $z \gtrsim 10$.

As the IGM is ionized, the UV background forms and can suppress star formation (Susa 2008;

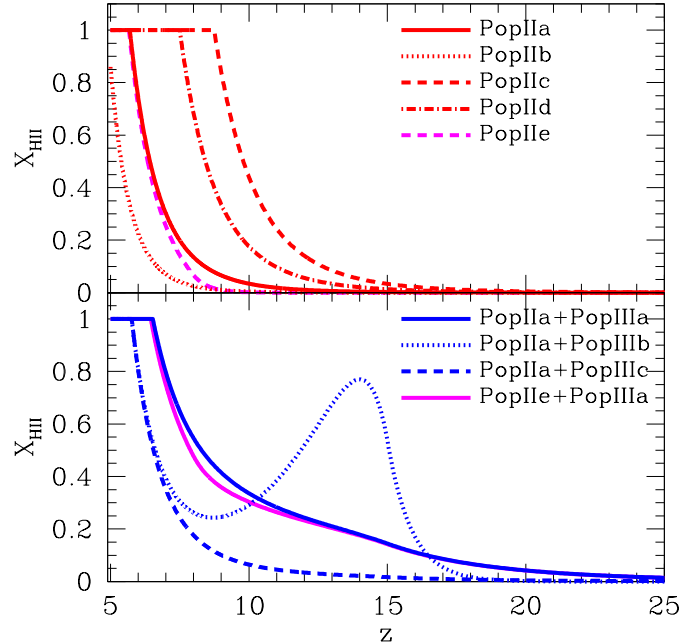


Figure 2. Redshift evolution of the ionization degree of the IGM with different models.

Faucher-Giguère et al. 2010; Yajima et al. 2012). Model PopIIId indicates that gas in galaxies is efficiently converted into stars, leading to a stronger UV radiation field. Recently Hasegawa & Semelin (2013) showed that the SFRD is self-regulated by external and internal UV feedback in cosmological radiation-hydrodynamics simulations. Their simulated SFRD is similar to our model PopIIa. In addition, Johnson et al. (2013) presented a co-evolution model of the SFRD for Pop II and III stars within a cosmological simulations including metal enrichment and radiative feedback. The SFRD of Pop III stars in their calculations is rather flat as a function of redshift which is similar to our models PopIIIa and PopIIIc. Their results show a Pop II SFRD that steeply increases with decreasing redshift which is similar to our PopIIa and PopIIc models.

3.2 Thomson scattering optical depth

The ionization histories in terms of the Thomson scattering optical depth (τ_e) for the different models is shown in Fig. 3. A subset of the models, most notably models with high PopII or PopII+PopIII star formation at $z > 10$, are in good agreement with the observational limits by the CMB (Komatsu et al. 2011; Planck Collaboration XVI 2014). Inclusion of PopIII stars proves to be important due to their top heavy IMF and the associated higher contribution of ionizing photons per stellar mass formed. Increasing the PopIII star formation rate by one order of magnitude at all redshift increases the optical depth in model PopIIa+PopIIIc from $\tau_e = 0.052$ to 0.087 . The optical depth from PopII stars only in this model is $\tau_e = 0.048$. The upper limit PopII-only model PopIIId is agreeing as well with the observational limits on τ_e owing to its high star formation rate. In principle

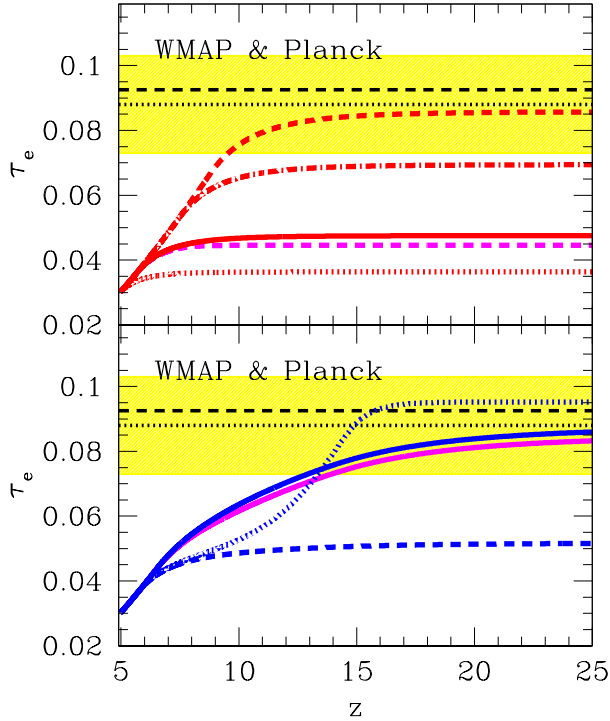


Figure 3. Thomson scattering optical depth for the same models shown in Figure 2. Black dashed and dotted lines are the observational data by WMAP (Komatsu et al. 2011) and Planck (Planck collaboration 2013) with the error of WMAP shown in yellow shade.

the uncertainty in the star formation history at $z \geq 9$ allows for some of these models to boost the ionization fraction at $z \geq 9$ by increasing the star formation history. Our results suggest, that the lower limit PopII star formation rate model PopIIa is not able to catch up with the CMB limits even if it would reach star formation rates similar to those in the upper limit model PopIIc at $z \geq 9$. The fact that the optical depth is an integrated quantity over redshift results in a certain degree of smearing out of the different ionization histories. This is most apparent for the models PopIIa+PopIIIa and PopIIa+PopIIIb which have $\tau_e = 0.087$ and 0.095 , respectively. The latter degeneracy makes the optical depth only a limited probe of the ionization history of the universe. As we will show in section 3.4 this degeneracy can be broken using 21 cm tomography.

In this work, we fix f_{esc} based on recent simulations, and investigate the 21 cm signal for different SFRD models. However, f_{esc} is highly uncertain due to the small sample of observed galaxies from which ionizing flux is detected (Iwata et al. 2009). Previous work investigating f_{esc} for fixed SFRD from simulations or observations (e.g., Wyithe et al. 2010; Paardekooper et al. 2013; Jaacks et al. 2013), finds f_{esc} of $\sim 0.05 - 0.5$ depending on the model. The ionization history is degenerate in SFRD and f_{esc} as $\dot{n}_{\text{Ion}}^{\gamma} \propto \text{SFRD} \times f_{\text{esc}}$. A possible way to break this degeneracy is by combining the ionization history with δT_b in future observations to get an accurate estimate of f_{esc} .

3.3 Spin temperature

Figure 4 shows the redshift evolution of CMB, gas and spin temperature in different models. The CMB temperature shows the expected cosmological $\propto (1+z)$ evolution, while the gas adiabatically cools via $\propto (1+z)^2$. Once X-ray heating from supernovae is included in our models, the gas temperature gradually increases with increasing cosmic star formation rate exceeding the CMB temperature at lower redshifts. The gas temperature is going in tandem with the ionization history due to their mutual dependence on massive stars either providing ionizing photons or type II supernovae. Similar as in the case of the ionization history discussed in the previous section the heating rate depends on the amount of PopII and PopIII star formation, with the models PopIIa+PopIIIa and PopIIa+PopIIIb exceeding the CMB temperature at $z \gtrsim 11$. The impact of Pop III star formation is highlighted again in the model PopIIa+PopIIIc, in which gas catches up to the CMB temperature only at $z = 7.7$. This is close to the expected redshift of $z = 7.5$ without any Pop III contribution in this model. In contrast the upper-limit Pop II star formation model predicts $z = 10.4$ as the redshift at which the excess starts.

As the gas is heated by X-ray photons, the spin temperature T_S starts deviating as well from T_{CMB} because both, X-ray and Ly α photons are proportional to the SFR. It stays close to the gas temperature T_{gas} because of a high Ly α background. At $z \gtrsim 15$ this is due to recombinations in HII regions generated by Pop III stars. Once Pop II star formation dominates at $z \lesssim 15$, the main source becomes continuum photons from stellar radiation. The small bump of T_S at $z \sim 15$ in model PopIIa+PopIIIa is due to our assumptions about the emission of Ly α photons from the ISM which is turned off at $z \sim 15$ as will be explained further in what follows. The coupling between T_S and T_{gas} depends on the intensity of the Ly α radiation field as e.g. seen in model PopIIa+PopIIIc where it is weaker at $z > 10$.

We present in Figure 5 the detailed redshift evolution of the coupling coefficients for Ly α scattering x_α and gas collisions x_C . As shown in Equation 14 for values larger than unity for either coupling coefficients, the spin temperature is close to the gas temperature resulting in either positive or negative 21 cm signals. The coupling constant for collisions x_C is always less than unity independent of the star formation model as it is driven by the density of the IGM, which is too low at the shown redshifts. Gas collisions thus play no important role in shaping the 21 cm signal at these redshifts. x_α on the other hand is larger than unity at low redshifts for most of the models suggesting a strong coupling between T_S and T_{gas} . Depending on the star formation model the contributions to x_α are either dominated by recombinations in the ISM or continuum radiation from stars. The recombination signal from the IGM is always below that from the ISM and plays a minor role. The dominance of continuum radiation over ISM recombinations is closely related to the dominance of Pop II star formation over Pop III star formation because of the SED shape of Pop II stars which peaks at wavelengths beyond the Lyman limit. As seen in the PopIIa+PopIIIa and PopIIa+PopIIIb models, x_α sharply drops down at $z \sim 15$ because of the way we model Ly α photons from the ISM. For model PopIIa+PopIIIa, the SFRD of Pop II stars stays above that of Pop III stars at

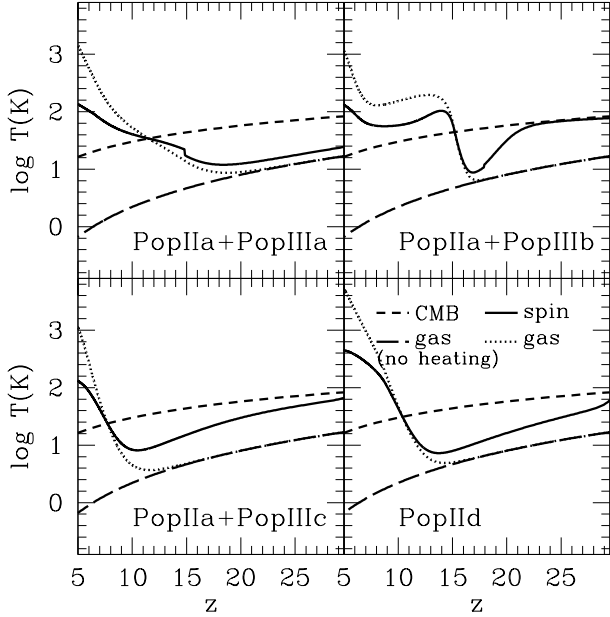


Figure 4. Redshift evolution of spin temperature with different models. Dot and dash lines are gas and CMB temperature, i.e., $2.7 \times (1+z)$ K, respectively. Long dash lines are gas temperature without heating by stellar sources, i.e., only expansion cooling is considered in Equation 7.

$z \sim 15$, while X_{HII} becomes larger than 0.5 at $z \sim 15$ in the case of model PopIIa+PopIIIb. Therefore, the contribution from Ly α photons from ISM is turned off. This artificial model also affects the redshift evolution of the 21 cm signal, but it is negligible as shown in the next section.

3.4 The 21 cm emission

Using the result from the previous sections we here derive the differential brightness temperature of the 21 cm line as a function of redshift. Figure 6 shows the differential brightness temperature δT_b for different models. The colored regions show the ranges covered by LOFAR and SKA. Models PopIIa and PopIIa+PopIIIc fail to reproduce the observed value of $\tau_e \sim 0.048 - 0.052$ and have $\delta T_b < 0$ even at $z \lesssim 10$. Our models that match the observed limits on τ_e show $\delta T_b > 0$ at $z \lesssim 10$, which is due to T_S and T_{gas} being higher than the CMB temperature. Note however, $\delta T_b \sim 0$ for model PopIIId at $z \lesssim 9$ because of the high ionization degree of the IGM. In contrast models PopIIa+PopIIIa and PopIIa+PopIIIb show $\delta T_b > 1$ down to $z \sim 6 - 7$ because parts of the IGM stay neutral, which matches the expectations from recent observations of LAEs that suggest some fraction of the IGM is still neutral at $z \sim 6.6$ (Kashikawa et al. 2011). However, a very small fraction of neutral hydrogen distributed around LAEs may change the Ly α flux and profile, leading to an underestimation of the ionization degree of IGM. The δT_b of PopIIe+PopIIIa is very similar to that of PopIIa+PopIIIa. Hence, it suggests that the different SFRD of PopII stars at $z > 8$ cannot be resolved by the 21 cm signal for the case that Pop III stars are dominant ionizing sources. The bump of δT_b in model

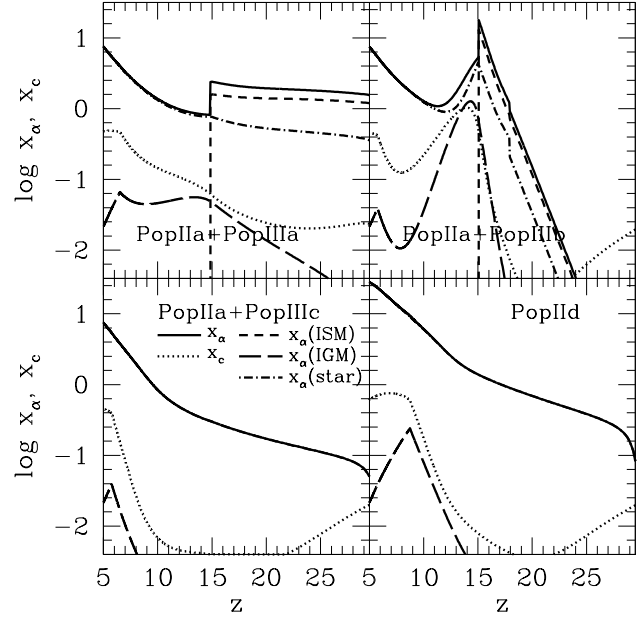


Figure 5. Redshift evolution of coupling coefficients. Solid and dotted lines are by Ly α scattering and gas collision respectively. Dashed, long-dashed and dot-dashed lines are the coupling coefficients for Ly α photons considering recombination in the ISM or IGM, or stellar continuum radiation alone, respectively.

PopIIa+PopIIIa at $z \sim 15$ is a result of the ceasing Ly α photons from the ISM which makes the coupling of T_S with T_{gas} weaker. In addition, we calculate δT_b without Ly α photon contribution from the ISM for models PopIIa+PopIIIa and PopIIa+PopIIIb in which the Ly α photons from the ISM control T_S significantly at $z \gtrsim 15$ as shown in Figure 5. As a result, at $z \gtrsim 15$ the coupling of T_S with T_{gas} becomes somewhat weaker, and the absolute values of δT_b decrease by factor ~ 2 . However, the trends for the redshift evolution of δT_b does not change.

The redshift evolution of our model PopIIId is similar to that in previous studies (Furlanetto 2006; Mirocha et al. 2013), i.e., $\delta T_b \sim 0$ at $z \gtrsim 20$, then negative due to the coupling of T_S and the low gas temperature with respect to the CMB, positive at $z \sim 10$ due to the heating, and $\delta T_b \sim 0$ at $z \sim 6$ due to complete reionization of the IGM. This evolution is clearly distinct to the one in our models including Pop III stars. As shown in Table 3, the gas temperature in the models with Pop III stars exceeds the CMB at higher redshift due to the efficient heating. Therefore, models with efficient Pop III star formation, PopIIa+PopIIIa or PopIIa+PopIIIb, show earlier transitions of δT_b from negative to positive compared to the models PopIIa+PopIIIc and PopIIId. The models with high Pop III SFR show that $\delta T_b \gtrsim -50$ mK at $z \sim 15$, while Pop II stars alone does deep absorption $\delta T_b \sim -170$ mK. In addition, if there is a strong peak in the Pop III star formation and the IGM is reionized twice (Cen 2003), the transition of δT_b is sharp, which can be used as a signal for a burst in Pop III star formation.

Future or ongoing 21 cm observation will give us information about the redshift evolution of δT_b . LOFAR will cover the frequency range of 115 – 180 MHz for the Epoch

of Reionization project¹, which will be corresponding to the 21 cm signal from the IGM at $6.9 \lesssim z \lesssim 11.4$. In our models, Pop II stars are the dominant sources of ionization and heating at these redshifts. Hence it is difficult to disentangle the SFH of Pop III stars from LOFAR data alone. On the other hand, SKA will cover the frequency range of 50 – 300 MHz ($3.7 \lesssim z \lesssim 26.4$)² and be able to distinguish different models, e.g., the late transition in PopIIId and the sharp transition in PopIIa+PopIIIb. Thus measurements of δT_b via the 21 cm signal probe the SFH of Pop III and Pop II stars at high redshift.

4 DISCUSSION

4.1 X-ray heating from black holes

In this work we have so far focused only on the X-ray contribution from SNe. Accreting black holes (BHs) are another viable source of X-rays that can modify the 21 cm signal (e.g., Baek et al. 2010; Mirabel et al. 2011; Jeon et al. 2014). We approximate the contribution from black holes assuming they accrete close to the Eddington limit (Willott et al. 2010), and that the mass in BHs is $\sim 10^{-3}$ times the stellar mass, which is the local observed value (e.g., Marconi & Hunt 2003; Rix et al. 2004). The bolometric luminosity of the BH is then $L_{\text{Edd}} = 1.4 \times 10^{35} \text{erg s}^{-1} [M_{\text{star}}/M_{\odot}]$. The above luminosity is an upper limit given that feedback from the accreting black hole is able to reduce the accretion close to the black hole (Milosavljević et al. 2009; Alvarez et al. 2009; Li 2011; Park & Ricotti 2011). We take for the spectrum from the accretion disc around the black hole the following power-law (Laor & Draine 1993; Marconi et al. 2004; Hopkins et al. 2007),

$$\nu L_{\nu} \propto \begin{cases} \nu^{1.2} & \text{for } \log(\nu/\text{Hz}) \leq 15.2 \\ \nu^{-1.2} & \text{for } \log(\nu/\text{Hz}) > 15.2. \end{cases} \quad (17)$$

Only X-ray photons with $E > 1$ KeV contribute towards the heating as softer X-ray photons mostly ionize hydrogen and helium (Furlanetto 2006). The former consist of 1.3×10^{-3} the total energy in X-ray photons.

The evolution for δT_b is shown in Figure 7. Due to the heating by BHs, the gas temperature is higher, resulting in higher δT_b . However, for models with efficient Pop III star formation (PopIIIa and PopIIIb), the addition of heating from BHs does not alter the results significantly as the heating from Pop III supernovae dominates. In contrast, models PopIIa+PopIIIc and PopIIId show an increase in δT_b accompanied by the additional X-ray heating. For the model PopIIa+PopIIIc the lowest temperature changes only slightly from $\delta T_b = -112.0$ to -99.3 mK and the transition redshift from negative to positive δT_b changes from $z = 7.7$ to 9.1 . Even for the model with the highest Pop II star formation rate (PopIIId) the minimum temperature of δT_b changes from -170.3 to -153.4 mK. Considering that we assumed accretion at the Eddington rate on to the BHs

our results predict that BHs will not leave a significant imprint onto the 21 cm signal.

Recent observations indicate that the mass ratio of BHs to stellar mass in high-redshift galaxies might be larger than that of local galaxies (see a review by Kormendy & Ho 2013). Here we additionally investigate the case of a high ratio with $M_{\text{BH}}/M_{\text{star}} = 10^{-2}$ which is ten times larger than for local galaxies and predict the effects on the X-ray background. The dashed-dotted lines shows δT_b in this case. Except for the PopIIa+PopIIIb, X-rays from BHs significantly change the redshift histories of δT_b . In the case of PopIIa+PopIIIb, the IGM quickly changes from cold and neutral with low stellar mass (low x-ray heating rate) to a hot ionized state due to the rapid Pop III star formation at $z \sim 15$. Hence, without the BH X-ray heating, the IGM is heated up to higher temperatures than that of the CMB. At $z < 15$, the X-rays from BHs heat the IGM further up. However, once the temperature becomes much higher than the CMB, δT_b does not depend on the gas temperature significantly (see equation 13). Hence the impact of BHs is smaller than in other models. For model PopIIa+PopIIIa, the maximum δT_b changes from 8.0 to 15.0, and the minimum δT_b goes from -151.4 to -147.0 . The transition redshift also changes from 11.5 to 14.8. In addition, for model PopIIId, the maximum δT_b changes from 6.8 to 19.7, the minimum δT_b goes from -170.3 to -127.3 , and the transition redshift goes from 10.3 to 13.5. As a result, the PopIIId model roughly shows similar redshift evolution of δT_b as the models including Pop III stars due to the efficient X-ray heating. Therefore, in the case of very high BH mass to stellar mass ratios and Eddington limited accretion onto the black hole, it becomes difficult to distinct the SFRD of different populations due to the addition of another heating source.

4.2 Pop III IMF

The SN heating rate for Pop III stars in our model is ~ 17 times higher than that for Pop II stars based on our choice of IMF slope and range. The exact form of the latter is still heavily debated (Bromm et al. 2009; Susa 2013; Stacy & Bromm 2014), and we estimate its impact in the limiting case of assuming both PopIII and PopII have the same IMF. The dotted lines in Figure 7 show δT_b for models where the IMF of Pop III and Pop II stars are the same, i.e. models with lower heating rate from Pop III stars. Models PopIIa+PopIIIa and PopIIa+PopIIIb show the expected trend of negative δT_b down to lower redshifts compared to the fiducial models. The model with the gradual evolution of the Pop III star formation rate (PopIIa+PopIIIa) only heats the IGM to the CMB temperature by $z = 9$ in contrast to $z = 11.5$ in the fiducial model. Please note that in the “bursty” Pop III star formation rate model (PopIIa+PopIIIb) δT_b is still negative even at the point where the Universe is reionized in this model at $z = 14$. ($X_{\text{HII}} = 0.77$). The higher emissivity of ionizing photons by Pop III stars allows to ionize the IGM for lower star formation rates, respectively heating rates. The low Pop III star formation rate model (PopIIIc) only shows slight deviations due to the relatively small contribution from Pop III stars at any redshift.

¹ <http://www.lofar.org/astronomy/eor-ksp/lofar-eor-project/lofar-epoch-reionization-project>

² <https://www.skatelescope.org/technology/>

As shown above, the heating rate by SNe changes with the shape of the IMF. Figure 8 shows the ratio of X-ray

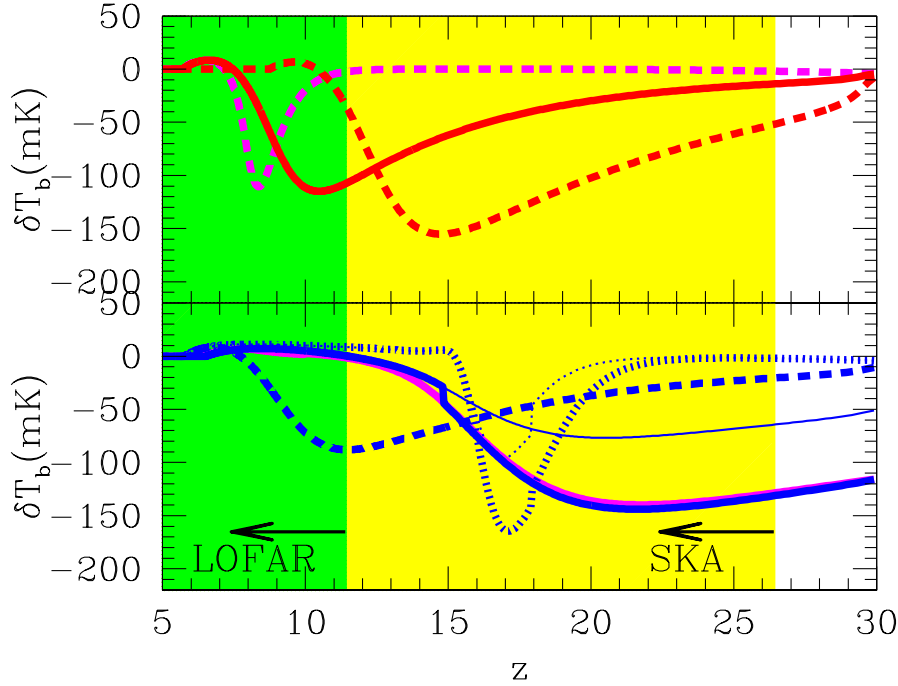


Figure 6. Redshift evolution of differential brightness temperature δT_b for different models as shown in Figure 2. Blue thin solid and dot lines represents the δT_b without Ly α photons from ISM. Shaded regions show the range covered by LOFAR ($z \lesssim 11.4$) and SKA ($z \gtrsim 26.4$).

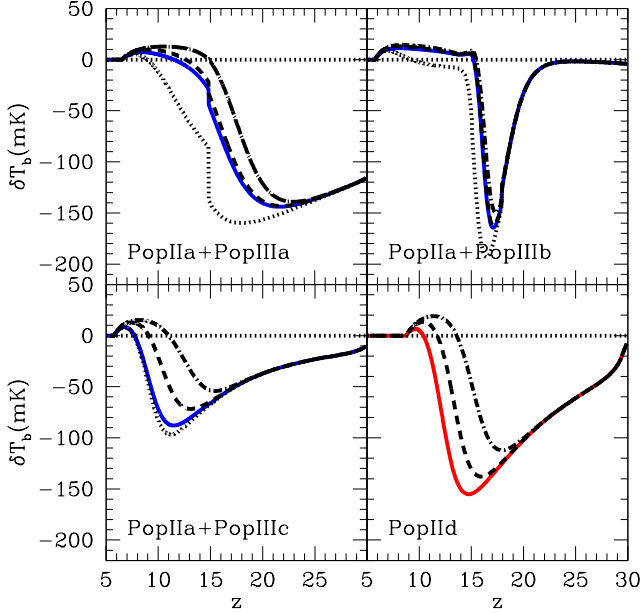


Figure 7. Redshift evolution of differential brightness temperature for different models. Solid lines are the same as in Figure 6. Dotted lines show the case in which we assume that the Pop III and Pop II IMF both are of Salpeter shape and range between $0.1 - 60 M_\odot$. Dashed and Dashed-dotted lines are the results for δT_b including X-ray heating from black holes with a mass ratio of $M_{\text{BH}}/M_{\text{star}} = 10^{-3}$ and $M_{\text{BH}}/M_{\text{star}} = 10^{-2}$, respectively.

luminosity from Pop III SN remnants to Pop II SN remnants for varying Pop III IMF slopes, $\frac{dn}{dM} \propto M^\alpha$, in the mass range of $10 - 500 M_\odot$. It has a peak at $\alpha \sim -1.2$, and decreases with α . The X-ray luminosity of Pop III stars is determined by the mass fraction settling into supernova and the number fraction between the core-collapse and pair-instability SN (Equation 6). At $\alpha = -1.2$, 0.58 per cent of stellar mass ends in core-collapse SN, and 22.7 per cent in pair-instability SN, resulting in the net energy of $E_{\text{SN}} = 2.2 \times 10^{52}$ erg per supernova.

Figure 9 summarises the redshift evolution of δT_b for different IMF slopes. As can be seen in the figure, the effect is not very strong for the different models. Model PopIIa+PopIIIa shows a slight shift towards higher redshifts at which $\delta T_b \sim 0$ in models with shallow slope $\alpha \sim -1$. Interestingly, for the model PopIIa+PopIIIb the IMF slope has only very weak impact on δT_b , even though the total mass in stars is comparable to the one in model PopIIa+PopIIIa. This is because partially ionized and heated gas phases are important for the 21 cm signal to distinguish the nature of the sources, however, the IGM quickly changes from cold and neutral state to a hot and highly ionized state. This results in a small impact of the IMF. Thus, it may be difficult to distinguish the IMF slope of Pop III stars by the 21 cm signal alone, even if the Pop III SFR is high and their contribution to cosmic reionization is large. However, the insensitivity of the signal to the IMF allows to derive robust estimates for the Pop III SFH.

In addition, the IMF of Pop III stars can control the SFRD of Pop II and III via metal enrichment from stars and supernovae. A higher X-ray heating model with $\alpha \sim -1$ is associated with efficient metal enrichment, resulting in

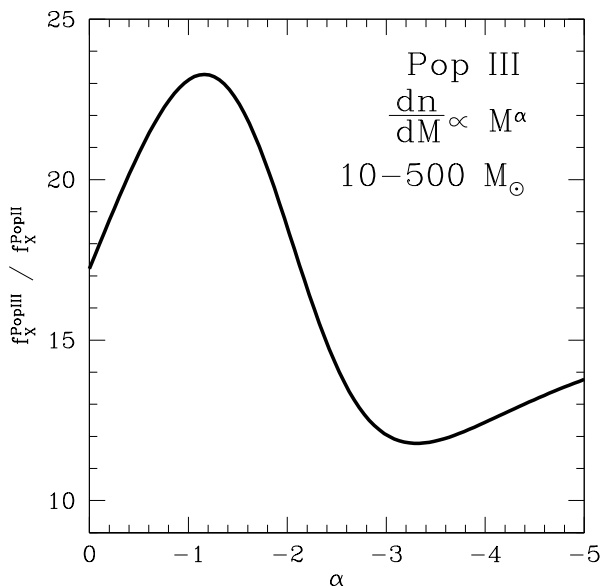


Figure 8. The ratio of X-ray luminosity from Pop III and Pop II SN remnants at the same SFR. The horizontal-axis shows the slope of the Pop III IMF, i.e., $\frac{dn}{dM} \propto M^\alpha$. The Pop III stars mass ranges from 10 to 500 M_\odot , and the Pop II from 0.1 to 60 M_\odot and has slope $\alpha = -2.35$.

suppression of Pop III star formation (Omukai et al. 2005). We will investigate the IMF, SFRD and the corresponding 21 cm signal in future work.

5 SUMMARY

Considering the present observational limits on the star formation rate in the high redshift Universe, we generated models of Pop II and Pop III star formation that are both consistent with these limits and the Thomson scattering optical depth of the cosmic microwave background. To break the degeneracy between these models we predict the expected 21 cm signal due to the heating of the IGM from SN remnants.

The limits on the SFR suggested by observed galaxies require high PopIII star formation rates to match the Thomson scattering optical depth. The cumulative mass of Pop III stars in this case is $\sim 10^6 M_\odot \text{ Mpc}^{-3}$ at $z \sim 6$. Note that, in this work, we have assumed an escape fraction of 0.5 for Pop III stars and 0.2 or 0.5 for Pop II stars based on recent numerical simulations (Yoshida et al. 2007; Wise & Cen 2009; Yajima et al. 2011, 2014; Paardekooper et al. 2013). These escape fractions can change the ionization history of the IGM and depend on halo mass (e.g., Yajima et al. 2011). If we use a high escape fraction of 0.5 for Pop II stars and the SFRD derived from GRB observations which take low mass galaxies below the detection limit of galaxies into account, Pop II stars alone can cause cosmic reionization and match the recent WMAP or Planck data without the need for Pop III stars.

Due to the different IMFs of Pop III and Pop II stars the SN rate per solar mass of stars formed is higher in the case of Pop III stars, as is the Ly α photons production, resulting in a different thermal history of the 21 cm signal compared

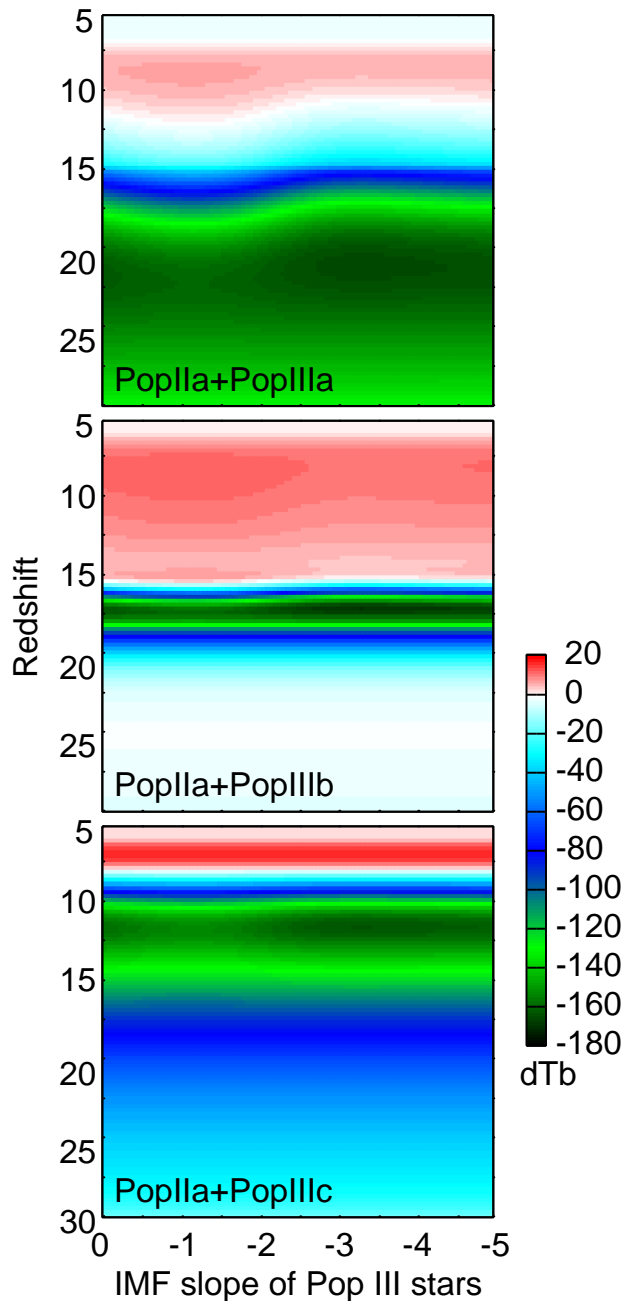


Figure 9. Two-dimensional map of the differential brightness temperature. The horizontal-axis is the slope of the initial mass function of Pop III stars, the vertical-axis shows the redshift.

to cases with Pop II stars alone. At $z \lesssim 10$, it is difficult to distinguish different SFR models, because most of gas are already ionized and heated up to temperatures higher than the CMB. On the other hand, at $z \gtrsim 10$, depending on the contribution of Pop III stars to cosmic reionization, the 21 cm signal shows very different histories. The models with high Pop III SFR show that $\delta T_b \gtrsim -50$ mK at $z \sim 15$, while Pop II stars alone does deep absorption $\delta T_b \sim -170$ mK. Upcoming missions such as the Square Kilometre Array (SKA) will cover redshifts up to $z \sim 20$, and hence are able to give constraints on the SFR of Pop III stars.

As well as SNe feedback, X-rays from BHs in galaxies can be heating sources of the IGM. We have studied the effect of BHs on the 21 cm signal with the assumption of the BH mass ratio to total stellar mass $M_{\text{BH}}/M_{\text{star}} = 10^{-3}$ and accretion at the Eddington rate. Our results show that BHs could heat up the IGM, however the impact on the 21 cm signal was not so significant. In addition, we investigated the effect of different slopes for the initial mass function of Pop III stars. The fraction of mass ending up in core-collapse and pair-instability SNe changes with the IMF slope. As a result, depending on the IMF slope, the heating rate by Pop III SNe changes. The heating rate has a peak at an IMF slope $\alpha \sim -1.2$. Hence, for the models with high Pop III SFR, the transition redshift that δT_{b} goes from negative to positive, becomes earlier at $\alpha \sim -1.2$. However, the effect of different α is not very strong making it difficult to infer the IMF slope by 21 cm observation even if the SFR of Pop III stars is high.

Here, we focused on the redshift evolution of the global 21 cm signal, i.e., the spatially mean value. In general the 21 cm signal significantly changes with the distance from ionizing/heating sources. We will study the inhomogeneous structure of the 21 cm signal by using detailed cosmological simulations in future works.

ACKNOWLEDGMENTS

We are grateful to Y. Li for valuable discussion. We thank the anonymous referee for useful comments.

REFERENCES

- Abel T., Bryan G. L., Norman M. L., 2002, *Science*, 295, 93
- Abel T., Wise J. H., Bryan G. L., 2007, *ApJ*, 659, L87
- Ahn K., Iliev I. T., Shapiro P. R., Mellema G., Koda J., Mao Y., 2012, *ApJ*, 756, L16
- Alvarez M. A., Pen U.-L., Chang T.-C., 2010, *ApJ*, 723, L17
- Alvarez M. A., Wise J. H., Abel T., 2009, *ApJ*, 701, L133
- Baek S., Di Matteo P., Semelin B., Combes F., Revaz Y., 2009, *A&A*, 495, 389
- Baek S., Semelin B., Di Matteo P., Revaz Y., Combes F., 2010, *A&A*, 523, A4
- Barkana R., Loeb A., 2001, *Phys. Rep.*, 349, 125
- Bouwens R. J., Illingworth G. D., Franx M., Ford H., 2007, *ApJ*, 670, 928
- Bouwens R. J. et al., 2011, *ApJ*, 737, 90
- Bouwens R. J. et al., 2012b, *ApJ*, 752, L5
- Bouwens R. et al., 2014, *ApJ*, 795, 126
- Bromm V., Ferrara A., Coppi P. S., Larson R. B., 2001a, *MNRAS*, 328, 969
- Bromm V., Kudritzki R. P., Loeb A., 2001b, *ApJ*, 552, 464
- Bromm V., Yoshida N., Hernquist L., McKee C. F., 2009, *Nature*, 459, 49
- Cen R., 2003, *ApJ*, 591, 12
- Chen X., Miralda-Escudé J., 2004, *ApJ*, 602, 1
- , 2008, *ApJ*, 684, 18
- Chongchitnan S., Silk J., 2012, *MNRAS*, 426, L21
- Ciardi B., Bolton J. S., Maselli A., Graziani L., 2012, *MNRAS*, 423, 558
- Clark P. C., Glover S. C. O., Smith R. J., Greif T. H., Klessen R. S., Bromm V., 2011, *Science*, 331, 1040
- Coe D. et al., 2013, *ApJ*, 762, 32
- Datta K. K., Friedrich M. M., Mellema G., Iliev I. T., Shapiro P. R., 2012, *MNRAS*, 424, 762
- Dewdney P. E., Hall P. J., Schilizzi R. T., Lazio T. J. L. W., 2009, *IEEE Proceedings*, 97, 1482
- Faucher-Giguère C., Kereš D., Dijkstra M., Hernquist L., Zaldarriaga M., 2010, *ApJ*, 725, 633
- Field G. B., 1958, *Proceedings of the IRE*, 46, 240
- Finkelstein S. L. et al., 2013, *Nature*, 502, 524
- Fioc M., Rocca V. B., 1997, *A&A*, 326, 950
- Furlanetto S. R., 2006, *MNRAS*, 371, 867
- Geil P. M., Wyithe J. S. B., 2008, *MNRAS*, 386, 1683
- González V., Labbé I., Bouwens R. J., Illingworth G., Franx M., Kriek M., 2011, *ApJ*, 735, L34
- Harker G. et al., 2010, *MNRAS*, 405, 2492
- Hasegawa K., Semelin B., 2013, *MNRAS*, 428, 154
- Heger A., Woosley S. E., 2002, *ApJ*, 567, 532
- Hirano S., Hosokawa T., Yoshida N., Umeda H., Omukai K., Chiaki G., Yorke H. W., 2014, *ApJ*, 781, 60
- Hirata C. M., 2006, *MNRAS*, 367, 259
- Hopkins P. F., Richards G. T., Hernquist L., 2007, *ApJ*, 654, 731
- Hosokawa T., Omukai K., Yoshida N., Yorke H. W., 2011, *Science*, 334, 1250
- Iliev I. T., Mellema G., Shapiro P. R., Pen U.-L., Mao Y., Koda J., Ahn K., 2012, *MNRAS*, 423, 2222
- Inoue Y., Inoue S., Kobayashi M. A. R., Makiya R., Niino Y., Totani T., 2013, *ApJ*, 768, 197
- Laursen P., Sommer-Larsen J., Razoumov A. O., 2011, *ApJ*, 728, 52
- Lonsdale C. J. et al., 2009, *IEEE Proceedings*, 97, 1497
- Iwata I., Inoue A. K., Matsuda Y., et al., 2009, *ApJ*, 692, 1287
- Jaacks J., Thompson R., Nagamine K., 2013, *ApJ*, 766, 94
- Jeon M., Pawlik A. H., Bromm V., Milosavljević M., 2014, *MNRAS*, 440, 3778
- Johnson J. L., Dalla V. C., Khochfar S., 2013, *MNRAS*, 428, 1857
- Johnson J. L., Khochfar S., 2011, *ApJ*, 743, 126
- Kashikawa N. et al., 2006, *ApJ*, 648, 7
- Kashikawa N. et al., 2011, *ApJ*, 734, 119
- Khochfar S., Silk J., Windhorst R. A., Ryan Jr. R. E., 2007, *ApJ*, 668, L115
- Kistler M. D., Yüksel H., Beacom J. F., Hopkins A. M., Wyithe J. S. B., 2009, *ApJ*, 705, L104
- Kistler M. D., Yüksel H., Hopkins A. M., 2013, *arXiv:1305.1630*
- Kitayama T., Yoshida N., Susa H., Umemura M., 2004, *ApJ*, 613, 631
- Komatsu E. et al., 2011, *ApJS*, 192, 18
- Kormendy J., Ho L. C., 2013, *ARA&A*, 51, 511
- Kuhlen M., Madau P., Montgomery R., 2006, *ApJ*, 637, L1
- Laor A., Draine B. T., 1993, *ApJ*, 402, 441
- Li Y., 2011, *arXiv:1109.3442*
- Liszt H., 2001, *A&A*, 371, 698
- Maio U., Khochfar S., Johnson J. L., Ciardi B., 2011, *MNRAS*, 414, 1145
- Marconi A., Hunt L. K., 2003, *ApJ*, 589, L21

- Marconi A., Risaliti G., Gilli R., Hunt L. K., Maiolino R., Salvati M., 2004, *MNRAS*, 351, 169
- Maselli A., Ferrara A., Ciardi B., 2003, *MNRAS*, 345, 379
- McLure R. J. et al., 2011, *MNRAS*, 418, 2074
- McQuinn M., Zahn O., Zaldarriaga M., Hernquist L., Furlanetto S. R., 2006, *ApJ*, 653, 815
- Mellema G., Iliev I. T., Pen U.-L., Shapiro P. R., 2006, *MNRAS*, 372, 679
- Mirabel I. F., Dijkstra M., Laurent P., Loeb A., Pritchard J. R., 2011, *A&A*, 528, 149
- Mesinger A., Furlanetto S., Cen R., 2011, *MNRAS*, 411, 955
- Milosavljević M., Couch S. M., Bromm V., 2009, *ApJ*, 696, L146
- Mirocha J., Harker G. J. A., Burns J. O., 2013, *ApJ*, 777, 118
- Nakamura F., Umemura M., 2001, *ApJ*, 548, 19
- Oesch P. A. et al., 2013, *ApJ*, 773, 75
- Oesch P. A. et al., 2014, *ApJ*, 786, 108
- Omukai K., Schneider R., Haiman Z., 2008, *ApJ*, 686, 801
- Omukai K., Tsuribe T., Schneider R., Ferrara A., 2005, *ApJ*, 626, 627
- Ono Y. et al., 2012, *ApJ*, 744, 83
- Ota K. et al., 2008, *ApJ*, 677, 12
- Paardekooper J.-P., Khochfar S., Dalla Vecchia C., 2013, *MNRAS*, 429, L94
- Park K., Ricotti M., 2011, *ApJ*, 739, 2
- Pawlik A. H., Schaye J., van Scherpenzeel E., 2009, *MNRAS*, 394, 1812
- Peebles P. J. E., 1993, *Principles of Physical Cosmology*
- Planck Collaboration XVI, 2014, *A&A*, 571, 16
- Pritchard J. R., Furlanetto S. R., 2006, *MNRAS*, 367, 1057
- Pritchard J. R., Loeb A., 2008, *Phys. Rev. D*, 78, 103511
- Pritchard J. R., Loeb A., 2010, *Phys. Rev. D*, 82, 023006
- Razoumov A. O., Sommer-Larsen J., 2010, *ApJ*, 710, 1239
- Rix H.-W. et al., 2004, *ApJS*, 152, 163
- Schaerer D., 2002, *A&A*, 382, 28
- Semelin B., Combes F., Baek S., 2007, *A&A*, 474, 365
- Shibuya T., Kashikawa N., Ota K., Iye M., Ouchi M., Furusawa H., Shimasaku K., Hattori T., 2012, *ApJ*, 752, 114
- Shull J. M., van Steenberg M. E., 1985, *ApJ*, 298, 268
- Stacy A., Bromm V., 2014, *ApJ*, 785, 73
- Stacy A., Greif T. H., Bromm V., 2012, *MNRAS*, 422, 290
- Stark D. P., Schenker M. A., Ellis R., Robertson B., McLure R., Dunlop J., 2013, *ApJ*, 763, 129
- Susa H., 2008, *ApJ*, 684, 226
- Susa H., 2013, *ApJ*, 773, 185
- Tokutani M., Yoshida N., Oh S. P., Sugiyama N., 2009, *MNRAS*, 395, 777
- Turk M. J., Abel T., O’Shea B., 2009, *Science*, 325, 601
- Umemura M., Susa H., Hasegawa K., Suwa T., Semelin B., 2012, *Progress of Theoretical and Experimental Physics*, 2012, 010000
- Whalen D., Abel T., Norman M. L., 2004, *ApJ*, 610, 14
- Willott C. J. et al., 2010, *AJ*, 140, 546
- Wise J. H., Abel T., Turk M. J., Norman M. L., Smith B. D., 2012a, *MNRAS*, 427, 311
- Wise J. H., Cen R., 2009, *ApJ*, 693, 984
- Wise J. H., Turk M. J., Norman M. L., Abel T., 2012b, *ApJ*, 745, 50
- Wouthuysen S. A., 1952, *AJ*, 57, 31
- Wyithe J. S. B., Hopkins A. M., Kistler M. D., Yüksel H., Beacom J. F., 2010, *MNRAS*, 401, 2561
- Wyithe J. S. B., Loeb A., 2007, *MNRAS*, 375, 1034
- Wyithe J. S. B., Loeb A., Barnes D. G., 2005, *ApJ*, 634, 715
- Yajima H., Choi J.-H., Nagamine K., 2011, *MNRAS*, 412, 411
- Yajima H., Choi J.-H., Nagamine K., 2012, *MNRAS*, 427, 2889
- Yajima H., Li Y., 2014, *MNRAS*, 445, 3674
- Yajima H., Li Y., Zhu Q., Abel T., Gronwall C., Ciardullo R., 2014, *MNRAS*, 440, 776
- Yajima H., Umemura M., Mori M., Nakamoto T., 2009, *MNRAS*, 398, 715
- Yoshida N., Oh S. P., Kitayama T., Hernquist L., 2007, *ApJ*, 663, 687
- Yoshida N., Omukai K., Hernquist L., 2008, *Science*, 321, 669
- Yüksel H., Kistler M. D., Beacom J. F., Hopkins A. M., 2008, *ApJ*, 683, L5
- Zheng W. et al., 2012, *Nature*, 489, 406